Effect of tissue optics on wavelength optimization for quantum dot-based surface and subsurface fluorescence imaging

Mathieu Roy
Farhan Dadani
Carolyn J. Niu
Anthony Kim
Brian C. Wilson

Effect of tissue optics on wavelength optimization for quantum dot-based surface and subsurface fluorescence imaging

Mathieu Roy,[a,b] Farhan Dadani,[b] Carolyn J. Niu,[b] Anthony Kim,[a,b] and Brian C. Wilson[a,b]
[a]University of Toronto, Ontario Cancer Institute, Department of Medical Biophysics, 610 University Avenue, Toronto, Ontario, M5G 2M9 Canada
[b]University Health Network, Ontario Cancer Institute, 610 University Avenue, Toronto, Ontario, M5G 2M9 Canada

Abstract. Optimization is an important but relatively unexplored aspect of contrast-enhanced fluorescence imaging, since minimizing contrast agent usage reduces the associated cost and potential toxicity. In a previous study, the authors developed a quantitative experimental approach to optimize quantum dot (QD)-based imaging using homogenized liver as a model tissue. In this follow-up study, the authors further extend and validate the approach using eight different tissues and five QDs emission wavelengths, and introduce quantitative imaging performance metrics, namely the threshold QD concentration and wavelength optimization gain. These metrics allow quantification of the improvements through spectral optimization in terms of reduced QD dose and identify the conditions that make the optimization process worthwhile. The authors show that, for most tissues, the most important parameter to optimize is the emission wavelength, yielding improvements of up to four orders of magnitude, followed by the excitation wavelength (up to 20-fold improvement) and the excitation filter bandwidth (up to 50% improvement). The authors also observe, by means of the optimization gain metric, that tissues exhibiting both high autofluorescence and strong pigmentation are generally better candidates for excitation wavelength optimization. This work contributes to the development of robust and quantitative dosimetry for QD-based fluorescence imaging near to the tissue surface. © *2012 Society of Photo-Optical Instrumentation Engineers (SPIE).* [DOI: 10.1117/1.JBO.17.2.026002]

1 Introduction

Quantum dots (QDs) are luminescent semiconductor nanoparticles with potential as contrast agents for medical imaging.[1] Their unique optical photophysical properties (broad excitation, narrow emission bandwidth, low photobleaching, and size-tunable emission wavelength) make them potential candidates for multiplexed reporting of biomarkers *in vivo*,[2] leading to applications in early cancer detection,[3] particularly endoscopically, and fluorescence-guided surgery.[4] Unfortunately, compared to existing fluorescent labels, they are relatively expensive, and there are significant toxicity concerns due to their elemental composition.[5]

To minimize cost and toxicity, it is imperative to optimize the use of QDs and obtain as much fluorescence contrast with the smallest possible dose.[6] Given their broad excitation spectrum and size-tunable emission, the excitation and emission wavelengths are two main parameters that require optimization. However, as previously discussed,[7,8] selecting the optimal excitation and emission wavelengths is complex, since the ability to detect QDs at depth in tissue and the tissue autofluorescence background both depend strongly on the tissue optical absorption and scattering properties,[9] which are themselves functions of wavelength.

To address this challenge, we have developed an experimental method, consisting of imaging a QD-loaded capillary tube embedded in homogenized tissue, together with a numerical model of light propagation in tissue to quantify the QD contrast versus relevant imaging parameters, such as the excitation and emission wavelengths and target depth.[10] In a previous study, we demonstrated the validity of this approach using artificial liquid phantoms of known optical properties and homogenized liver as a proof-of-principle model tissue. This led to the following provisional conclusions regarding contrast optimization: 1. it is advantageous for surface imaging to use an excitation wavelength corresponding to a tissue absorption peak, since this reduces the tissue autofluorescence background and 2. the contrast falls rapidly with depth of the QDs, at a rate that increases predominantly with tissue absorption, leading to spectral shifts and overall flattening of the spectral contrast.

However, since that study used only one tissue type, the generalizability of these conclusions for optimizing QD-based bioimaging remains to be established. Here, the same approach is expanded to four different homogenized tissues and four representative hollow organs, using QDs emitting at five different emission wavelengths and, for comparison, matched fluorescent dyes.

In addition to providing further insight into QD image optimization, these studies allow more complete validation of the phantom and modeling methods. Thorough validation requires variation of numerous parameters, including the target fluorescence spectra and depth z, the excitation λ_{ex} and emission wavelength λ_{em}-dependent tissue absorption μ_a, reduced scattering μ_s' and autofluorescence (AF), and the dilution of the tissue

Address all correspondence to: Brian C. Wilson, University of Toronto, Ontario Cancer Institute, Department of Medical Biophysics, 610 University Avenue, Toronto, Ontario, Canada M5G 2M9. Tel: 416-946-2952; Fax: 416-946-6529; E-mail: wilson@uhnres.utoronto.ca

homogenate. However, attempting to cover each in detail is beyond the scope of this article. For example, the effects of target depth and tissue dilution were well documented in our first study, and so will not be presented in detail here. Hence, for the sake of brevity, we only briefly present the final results of the validation study, and focus instead on the challenge of optimizing the image contrast. For this, we introduce novel performance metrics, namely the threshold QD concentration c_{th} and wavelength optimization gain G, as measures of the potential impact of optimization on minimizing the dose of QDs required to achieve adequate target contrast.

2 Methods

2.1 QD and Fluorophore Preparation

(CdSe)ZnS QDs emitting at peak wavelengths of 500, 550, 600, and 650 nm and dispersed in chloroform were prepared using a well-established organometallic procedure.[11] Qdot 705, Alexa-Fluor488, AlexaFluor532, AlexaFluor568, AlexaFluor633 and AlexaFluor680 were used as purchased (Q21361MP A-20000 A-20001 A-20003 A-20005 A-20008, Invitrogen, Carlsbad, California). QD excitation and emission fluorescence spectra (Fig. 1), and absorption spectra were acquired using a scanning spectrofluorometer (Fluorolog 3, Horiba Jobin-Yvon, Edison, New Jersey, USA) and a UV-Vis spectrometer (Cary 300, Varian, Inc. Palo Alto, California, USA), respectively. The quantum yield of each was calculated as the total emitted fluorescence divided by the absorption coefficient at 385 nm for the QDs and at 488, 532, 568, 633, and 680 for the organic dyes. The values were then normalized to the known (0.92) quantum yield of AlexaFluor488.

The concentrations were determined from the absorption spectra, following a method developed by Yu et al.[12] for the QDs and using Beer's law (with molar extinction coefficients published by Invitrogen) for the dyes.

2.2 Tissue Preparation

The previous study used porcine liver tissue for proof-of-principle validation of the contrast optimization approach.[10] Here, in order to validate the method further using tissues with a range of optical properties, fresh (not previously frozen) porcine kidney and liver, and bovine brain and lung were used. Each tissue was homogenized and diluted following the previous protocol.[8] All bulk tissues were processed and imaged within 12 h of acquisition.

In addition, to add clinical relevance, four different hollow organs—bladder, colon, esophagus, and stomach—were included. These were excised immediately post mortem from a healthy, 70 kg female Yorkshire Cross pig. For logistics reasons, these were collected some weeks before the imaging experiments and stored at −70 °C. Prior to imaging, the organs were gently cleaned with saline and a 1 cm² flap of mucosa plus submucosa was surgically separated from the underlying muscle layer. This allowed both surface and subsurface fluorescence imaging within the same region of interest, as depicted in Fig. 2. The thickness of the mucosa + submucosa was estimated mechanically and optically for each tissue using a Vernier caliper and confocal microscopy as 700 ± 50, 400 ± 50, 800 ± 100, 2000 ± 200 μm for the bladder, colon, esophagus, and stomach, respectively. These values are in reasonable agreement with the literature,[13–16] considering that the thickness of the colon depends on the degree of stretching.

To avoid degradation, all tissues were refrigerated between manipulations and intact tissues were regularly re-hydrated with isotonic saline during the imaging procedure.

2.3 Tissue Optical Property Measurements

Tissue optical properties were acquired using a 1 mm diameter diffuse reflectance fiber-optic spectrometry probe that has an accuracy of $\pm 10\%$ in this spectral range.[17] The diffuse reflectance at 3 fiber source-detector separations were processed using an inverse Monte Carlo algorithm, combined with a priori knowledge of the spectral signature of the main absorbers, namely oxy- and deoxyhemoglobin and a simple inverse dependence for the scattering. The measured absorption and reduced scattering spectra for the 100% homogenates and hollow organs are shown in Fig. 3. The uncertainty on these measurements, including both the probe's precision and tissue spatial variations, is approximately $\pm 15\%$ and $\pm 20\%$ for the homogenized and intact tissues, respectively. Note that the pigment packaging effect[24] was partially taken into account by feeding the diffuse reflectance model with measurements of oxygenated and deoxygenated whole blood absorption spectra rather than hemoglobin spectra from the literature. However, better optical property estimates could likely be obtained by including the pigment packaging effect to our model.

2.4 Fluorescence Imaging and Image Analysis

Fluorescence imaging was performed using a custom-made multi-spectral imaging system consisting of an epifluorescence
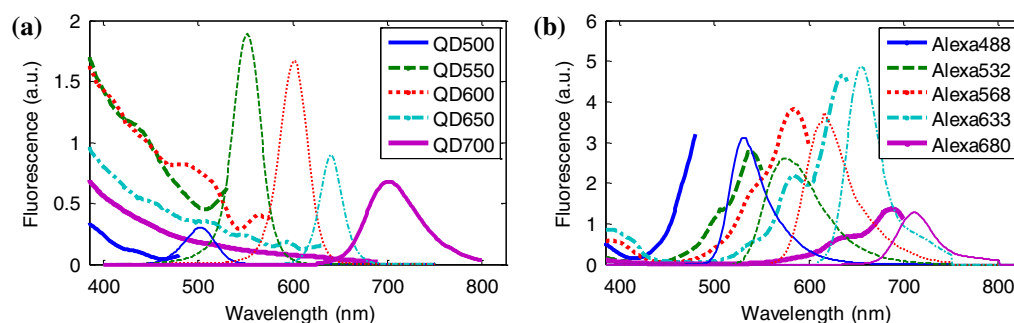
Fig. 1 Fluorescence excitation (thick) and emission (thin lines) spectra for (a) the QDs and (b) the corresponding AlexaFluor dyes. The concentrations were adjusted to match the absorption spectrum at 385 nm for the QDs and the peak absorption of the dyes (488, 532, 568, 633, 680). The calculated quantum yields were 0.16, 0.75, 0.58, 0.24, 0.39 for the QDs and 0.92, 0.52, 0.77, 0.53, 0.17 for the dyes.
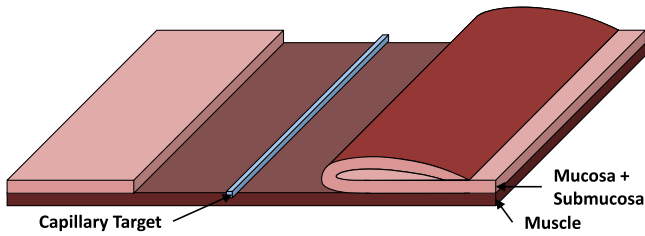
Fig. 2 Schematic of a hollow organ after separation of the mucosa from the underlying muscle or cartilage layer. For subsurface imaging, the capillary target is placed on the muscle layer and the mucosa and submucosa are folded back. For surface imaging the capillary is placed on top of the mucosa.

stereomicroscope (MZFLIII, Leica Microsystems, Richmond Hill, Ontario, Canada), cooled CCD camera (CoolSNAP K4, Photometrics, Tucson, Arizona, USA) and automated excitation and emission filter wheels (AB304-T, Spectral Products, Putnam, Connecticut), as previously described in detail.[10] All measurements were done under high signal-to-noise conditions, using 12 excitation filters ranging from 385 to 620 nm (average bandwidth 20 nm) and five emission filters corresponding to the QD emission peaks at 500, 550, 600, 650, and 700 nm (bandwidth 50 nm). Images were corrected for the camera noise, excitation lamp spectrum, exposure time and spatial illumination profile, and analysed as previously described.[10] The measured image contrast, or target-to-background ratio (TBR), is defined as the ratio of fluorescence signals emitted by the target (in this case the QD-filled capillary) and background regions of interest:

$$X_{\text{TBR}} = X_{\text{TR}}/X_{\text{BR}}. \qquad (1)$$

3 Model Extension

The original Monte Carlo model[10] used the target and tissue absorption, scattering and fluorescence spectra as inputs, and had two main outputs: the tissue autofluorescence as a function of homogenate dilution, and the target signal versus depth. Here, we extend the model to include specific performance metrics, namely the threshold QD concentration c_{th} and the wavelength optimization gain G. As described below, c_{th} is derived from the TBR, but includes a normalization factor for the target concentration, thus allowing absolute contrast comparisons.

3.1 Threshold Concentration (c_{th})

We showed previously[10] that the TBR may be expressed as follows:

$$X_{\text{TBR}} \cong \frac{X_{\text{QD}} + F_{\text{MC}}}{F_{\text{MC}}}, \qquad (2)$$

$$X_{\text{QD}} = X'_{\text{QD0}} F_{\text{ex,em}}(z_c)(1 + R_{\text{ex}}), \qquad (3)$$

where X'_{QD0} is the background-free QD signal obtained from a direct measurement of the capillary target, and R_{ex}, $F_{\text{ex,em}}(z_c)$, and F_{MC} were obtained by Monte Carlo simulation and represent the excitation light backscattering factor, depth-dependent attenuation factor and predicted autofluorescence signal, respectively. Since X'_{QD0} increases linearly with QD concentration, X_{QD} can be expressed as

$$X_{\text{QD}} = c_{\text{QD}} x_{\text{QD}}, \qquad (4)$$

where c_{QD} is the QD concentration and x_{QD} is the fluorescence per unit concentration. Here the objective is to quantify how much the required QD concentration can be reduced by optimizing key imaging parameters, so we define a threshold TBR_{th} and estimate the required QD concentration to reach this threshold from Eq. (2):

$$c_{\text{th}} = (\text{TBR}_{\text{th}} - 1)\frac{F_{\text{MC}}}{x_{\text{QD}}}. \qquad (5)$$

One challenge of this work was to define a criterion for the minimum detectable contrast. The Rose criterion,[25] stating that the signal-to-noise ratio (SNR) of 5 is needed to detect a signal with 100% certainty, was considered but could not be directly applied to our situation since our images are typically acquired with high SNR (~50 to 200 in most cases). Thus, in the absence of a generally-accepted contrast standard for high SNR images, an arbitrary value of $\text{TBR}_{\text{th}} = 2$ was selected as the minimum to achieve detectable contrast. Note that selecting a higher value does not substantively alter the conclusions reached below, except for scaling of the QD concentrations, by a factor $\text{TBR}_{\text{th}} - 1$. Thus,

$$c_{\text{th,best}} = \frac{F_{\text{MC}}(\lambda_{\text{best}})}{x_{\text{QD}}(\lambda_{\text{best}})}, \qquad (6)$$

$$c_{\text{th,broad}} = \frac{\sum_{\lambda_i} F_{\text{MC}}(\lambda_i)}{\sum_{\lambda_i} x_{\text{QD}}(\lambda_i)}, \qquad (7)$$

where $c_{\text{th,best}}$ and $c_{\text{th,broad}}$ are the QD concentrations required to obtain TBR = 2 using a single (optimal) excitation wave-
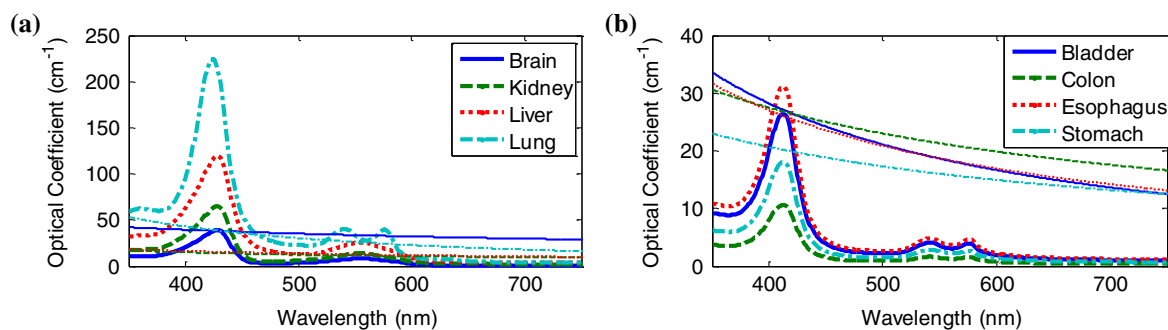
Fig. 3 (a) Absorption (thick) and reduced scattering (thin lines) spectra measured for the 100% homogenized bulk organs, and (b) for the intact hollow organs (measured from the mucosal side).

length and broadband illumination, respectively. The broadband illumination scenario was included to benchmark the wavelength optimization approach. Note that the threshold concentration for broadband excitation was not directly measured, but rather was estimated by summing the contributions from all excitation filters shorter than the emission wavelength minus 50 nm (to avoid leakage of excitation light to the detector). Since the 385 nm filter was used as the shortest wavelength in all cases, the effective bandwidths for the simulated broadband conditions were 85, 145, 185, 235, and 255 nm for detection at 500, 550, 600, 650, and 700 nm, respectively.

3.2 Wavelength Optimization Gain (G)

As a performance metric, the gain due to optimizing the wavelength is defined as the ratio between the threshold concentrations for the suboptimal and optimal illumination cases:

$$G_{\text{broadband}} = \frac{c_{\text{th,broad}}}{c_{\text{th,best}}}. \tag{8}$$

Similarly, the maximum gain between the worst wavelength choice and the optimized case is:

$$G_{\text{max}} = \frac{c_{\text{th,worst}}}{c_{\text{th,best}}}. \tag{9}$$

For the purpose of validating the model, the c_{th} and G predictions were compared to values extrapolated from the measurements, obtained by substituting x_{QD} by $(X_{\text{TR}} - X_{\text{BR}}/c_{\text{QD}})$ and F_{MC} by X_{BR} in Eqs. (5)–(7). Also, since the autofluorescence predictions were poor in some cases (see Sec. 4.1), a simplified model in which the autofluorescence was measured directly instead of being calculated, was used for all data presented here, except for Sec. 4.1. Thus, F_{MC} is simply replaced by X_{BR}, with x_{QD} unchanged.

4 Validation

As mentioned previously, the Monte Carlo contrast optimization model predicts the behavior of the tissue autofluorescence and the target signal (or contrast). In our previous study, the model was partially validated using artificial liquid phantoms, a single homogenized tissue (liver) and a single QD emission wavelength (600 nm). To test the model across a wider parameter space, we used eight different ex vivo tissues and five QD emission wavelengths. Here, we briefly present the conclusions in terms of autofluorescence and contrast predictions.

4.1 Autofluorescence Versus Tissue Dilution

First, the autofluorescence predictions were tested using four different homogenized tissues and five different emission wavelengths. To quantify the agreement between the measured and predicted autofluorescence versus dilution curves, the average reduced χ^2 coefficient (deviation to error ratio) for each tissue and emission wavelength was calculated, using a relative error of $\pm 20\%$ for the autofluorescence measurements (an upper boundary that includes all sources of noise as well as intra- and inter-sample variations). Most values were below 2, except for some of the lung homogenates and the brain tissue at 650 and 700 nm. Fig. 4 shows an example of good agreement between measured and predicted autofluorescence.
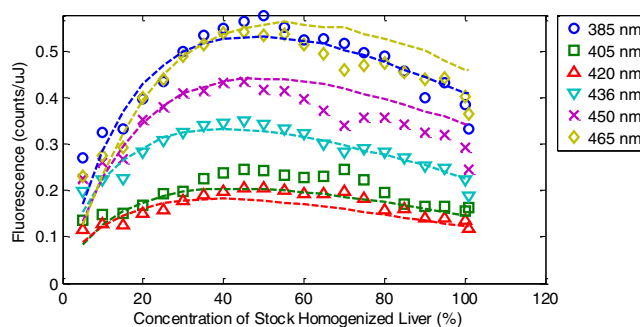
Fig. 4 Typical case (liver, $\lambda_{\text{em}} = 700$ nm) of good agreement between the measured (symbols) and predicted (dashed lines) autofluorescence versus concentration of homogenized tissue. The data for intact tissue are immediately to the right of 100% homogenized tissue points.

Further analysis of the problematic cases suggested that the discrepancies are related to experimental conditions rather than being limitations of the model itself. For example, in lung tissue, steep variations in the experimental data are likely due to *ex vivo* tissue manipulations, such as dilution errors, large temperature variations,[18] bacterial contamination of some samples or inter-sample variations due to differential blood oxygenation or blood retention. The model autofluorescence predictions were previously validated under fully controlled experimental conditions (using liquid phantoms of known optical properties). However, the accuracy of the predictions depends strongly on experimental inputs, such as the optical properties, being well determined. Since that was not the case for all tissues here, it was decided to use the directly measured AF data as being overall more accurate.

4.2 Accuracy of the Model's Contrast Predictions

To summarize the validation of the model predictions of image contrast, statistics were compiled for the optimal wavelength λ_{best} best, threshold concentration for optimal-wavelength illumination $c_{\text{th,best}}$ threshold concentration for broadband illumination $c_{\text{th,broad}}$, and wavelength optimization gain $G_{\text{broadband}}$. For each bulk tissue, measurements and predictions were made for 40 different cases: five emission wavelengths for both QDs and matching dyes for each of four tissue configurations (25% concentration, surface; 25%, 480 μm subsurface; 100%, surface; intact, surface). The hollow organ measurements were also included (four organs at five emission wavelengths for two contrast agents = 40 cases), both to increase the range of test cases and to assess the model predictions under more clinically (i.e., endoscopically) relevant conditions. For the subsurface configuration, 15 cases, including all 10 stomach measurements, were discarded because of low fluorescence signal. The validation results are summarized in Table 1.

The model was judged accurate if the error was <10 nm for the wavelength predictions and if the predicted value was within a factor of 1.6, arbitrarily chosen to yield a target overall success rate of ~80%. The poorest agreement was for the hollow organ/subsurface situation (due to the uncertainty on the measured thicknesses and weak target signals), for which the tolerance factor needed to be increased to 2.1 to achieve an 80% success rate. Thus, there is reasonable confidence that the model can predict the threshold concentration within a factor of 2 over a wide range of tissues and wavelengths.

Table 1 Percent of cases for each parameter in which the predictions were within a factor of 1.6 from the measurements.

	$\lambda_{best}(\%)$	$c_{th,best}(\%)$	$c_{th,broad}(\%)$	$G_{broadband}(\%)$	N Test
Brain	90	85	83	93	40
Kidney	85	85	88	98	40
Liver	90	90	80	95	40
Lung	85	68	65	98	40
Hollow surface	93	98	93	95	40
Hollow subsurface	64	56	48	64	25
Total	**86**	**82**	**78**	**92**	**225**

5 Optimization Results

Now that the model's validity has been demonstrated, we present the optimization results, primarily focusing on the effect of tissue optical properties on the threshold concentration. First, a typical example of the threshold concentration calculation is presented, followed by an analysis of the effects of the excitation and emission wavelengths.

5.1 Calculation of Threshold Concentrations

Fig. 5 shows a typical example of measured and calculated TBR spectra for a set of tissue samples, and how the variations in TBR translate to significant differences in the c_{th} values. The uncertainty in the threshold concentration stems from 1. the variability in the AF measurements taken at multiple regions of interest on the tissue sample, and 2. the uncertainty on the c_{QD} value, estimated to $\pm 10\%$, as suggested by Yu et al.[12]

In the example of Fig. 5, a simple change of excitation filter can reduce the threshold QD concentration by a factor 3.3 (intact tissue) to 6.6 (25%, subsurface). Similarly, using an optimized excitation filter instead of broadband illumination can reduce the required QD concentration 2- to 3-fold. These are straightforward instrumentation improvements that would translate into reduced cost and potential toxicity of the QD-based contrast agent. Note that the 25% subsurface case in Fig. 5(a) is a rare ($\sim$14%) instance of the model inaccurately predicting the

optimal wavelength, likely due to underestimating the absorption at 405 nm and failing to predict the shift of optimal wavelength from 405 to 510 nm. This red-shift effect of target depth is discussed further in Sec. 7.3.

5.2 Excitation Wavelength Optimization

Here, the contrast optimization is summarized in terms of optimal excitation wavelength. First, for each tissue sample, c_{th} was calculated at all excitation and QD emission wavelengths. Fig. 6 shows a typical example of c_{th} as a function of λ_{ex} and λ_{em}, and it is clearly observed that the QD emission wavelength has much greater influence on the threshold concentration values than does the excitation wavelength. This is due to the properties of endogenous fluorophores[19] and was observed for all tissue types, as shown below.

To remove the strong λ_{em} dependence, we normalized each curve by applying the transformation:

$$\frac{1}{G_{\lambda_{ex}}} = \frac{c_{th,best}}{c_{th}(\lambda_{ex})}, \quad (10)$$

thus emphasizing the excitation spectral shape. We refer to this normalization as the inverse gain, or simply "normalized contrast," due to its similarity with Eq. (8). Fig. 7 shows the inverse gain spectra for the bulk and hollow organs and for surface imaging conditions. Before discussing these data, it

	25% Kidney	100% Kidney	Intact Kidney	25% Subsurface
Worse Wavelength	0.48	0.57	0.30	2.42
Broadband	0.24	0.24	0.18	1.09
Optimal Wavelength	0.095	0.086	0.092	0.366
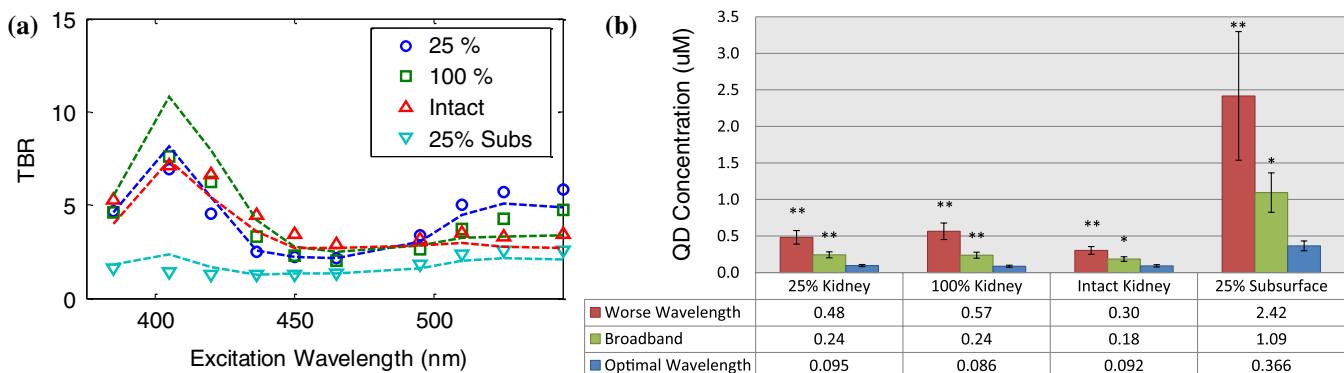
Fig. 5 (a) Measured (symbols) and modeled (dashed lines) TBR for 25%, 100%, intact and 25% subsurface (480 μm) imaging in kidney tissue. The true c_{QD} value was 4.0 μM. (b) c_{th} values calculated from Eq. (5) with $TBR_{th} = 2$, using broad (green) or narrow band illumination centered at the worst (red) or optimal (blue) excitation wavelength. The worst wavelength was 465 nm, and the optimal was 405 nm for surface and 510 nm for subsurface imaging. The c_{th} values were significantly higher when using broadband or worst wavelength illumination, with $p < 0.01$ (**) and $p < 0.05$ (*).
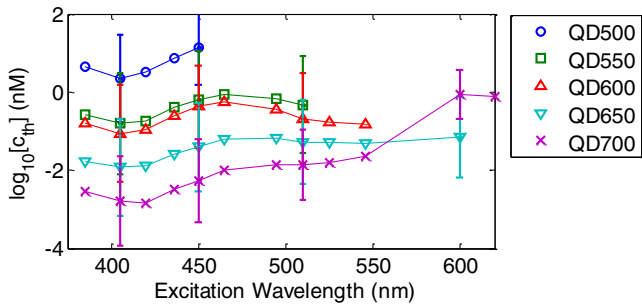
Fig. 6 Estimated threshold concentration (c_{th}) versus λ_{ex} for QDs emitting at different wavelengths. This particular data set corresponds to surface imaging of undiluted (100%) homogenized kidney tissue. The lines are simply to guide the eye. Typical error bars are shown.

is important to bear in mind that, due to the inherent difficulties of manipulating ex vivo tissues (see Sec. 7.1), the results may not be directly translatable *in vivo*. However, general trends, such as the spectral shapes, are expected to be maintained *in vivo*.

The normalized contrast spectra were closely related to the excitation spectrum of the contrast agent and the tissue autofluorescence, which is itself strongly affected by the tissue absorption spectrum. Moreover, the tissue backscattering ratio had negligible influence on the shape of these spectra. Most

tissues had a narrow optimization band, for all emission wavelengths, in the 395 to 425 nm region, corresponding to the main absorption peak of hemoglobin. This is important for clinical imaging applications, as it confirms that multiple QDs emitting at different wavelengths could be simultaneously excited optimally using a single excitation wavelength, which greatly facilitates multiplexed imaging of several biomarkers.

The lung, brain, and colon tissues had qualitatively different behavior than the other tissues. The colon had the lowest blood content, as confirmed by its low absorption spectrum [Fig. 3(b)], which translated into much less variation in autofluorescence and normalized contrast spectra. Although the lung and brain tissues had extremely different optical properties [Fig. 3(a)], their inverse gain spectra behaved similarly, exhibiting a shift in optimal wavelength from 405 towards 450 nm when using orange (600 nm), red (650 nm), and near infrared (700 nm) QDs. On average they had much lower AF intensity than the other tissues and the proportion of autofluorescence excited in the 420 to 550 nm region was less than the other tissues at 600 nm and negligible at 650 and 700 nm emission. This suggests perhaps not surprisingly that there are major differences in the intrinsic AF of brain and lung compared to the other tissues. Hence, although the wavelength optimization is driven by the hemoglobin absorption in most cases, the spectral signature of endogenous fluorophores and their relative concentration in tissues can also play a role.[19]
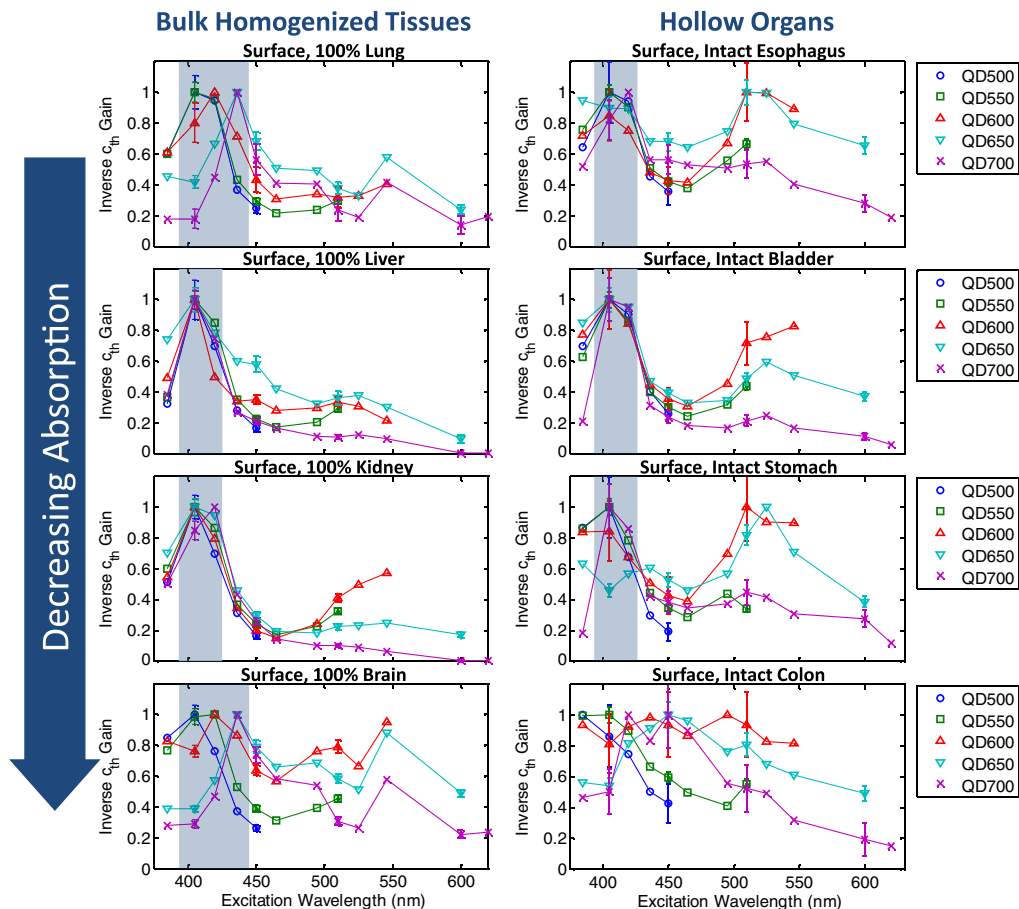
Fig. 7 Inverse gain (normalized contrast) versus excitation wavelength for different QD emission wavelengths (symbols), for surface imaging in homogenized tissue (left) and intact hollow organs (right). The shaded zones represent optimal excitation windows. The lines are simply to guide the eye.
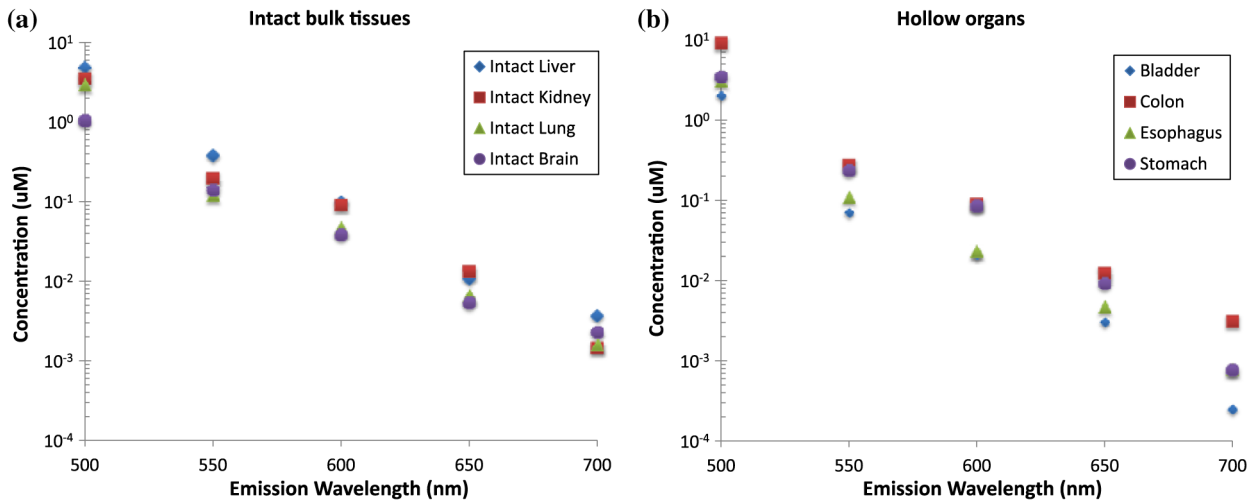
Fig. 8 Surface optimal QD threshold concentration versus emission wavelength for (a) intact bulk tissues and (b) hollow organs. Note the logarithmic concentration scale.

5.3 Threshold QD Concentration Versus Emission Wavelength

Fig. 8 shows how the optimized threshold concentrations vary with emission wavelength. It is a common claim[20] that it is better to use near-infrared imaging contrast agents, since the tissue autofluorescence background is lower, but this has not been validated quantitatively to date. The results here show that the dependence is indeed strong. Thus, for example, changing from 500 to 700 nm emitting QDs reduces the threshold concentration by up to four orders of magnitude for the hollow organs (from 2800-fold for the colon up to 8000-fold for the bladder), and 3 orders of magnitude for the bulk tissues (from 550-fold for the brain to 2400-fold for kidney). This is also true for the subsurface experiments, as discussed in Sec. 7.3. Another important finding is that all tissues behave similarly with respect to the emission wavelength, and that in general the threshold concentration exhibits stronger dependence on the emission wavelength than on the excitation wavelength or tissue type.

6 Applications to Biomedical Imaging

In this section, the effects of the wavelength optimization are quantified and the impact on contrast agent dose for potential clinical use is evaluated. For these purposes, the effect of tissue optical properties on the wavelength optimization gain metric is examined. We then discuss the implications for *in vivo* imaging in terms of cost savings, and demonstrate how this novel approach allows quantitative comparisons between different fluorescent contrast agents.

6.1 Gain Versus Tissue Optical Properties

In order to examine how the excitation wavelength optimization gain behaves with tissue optical properties, Fig. 9 shows the QD600 threshold concentration and corresponding wavelength optimization gain for all tissue types: note that $G = 1$ corresponds to no improvement and that, due to the relatively high uncertainties for the estimated concentrations (up to $\pm 30\%$), gain values lower than 2 are not statistically significant in most cases. Similarly, due to the large uncertainties, comparing

different gain values yields conclusions lacking statistical significance but still worth exploring here.

The threshold concentration and gain vary markedly with tissue type. As discussed in Sec. 5.2, the optimization gain depends on the tissue autofluorescence, which in turn is spectrally modulated by tissue pigmentation. Thus, highly fluorescent, strongly pigmented tissues exhibit the highest optimization gain values. It is also not surprising that the tissues with the lowest blood content (brain, colon) exhibit the lowest optimization gain. Finally, the lung, despite its strong pigmentation, is among the tissues with the lowest optimization gain, due to its very low AF at 600 nm.

6.2 Gain Versus Emission Wavelength

Figure 10 shows how the optimization gain varies with the QD emission wavelength for different tissues. The bladder, colon and brain tissues were chosen as representative of high pigmentation, low pigmentation, and spectrally variable intrinsic autofluorescence, respectively. In general, the optimization gain stays relatively constant with emission wavelength for all tissue types, except for slightly higher gain values at 700 nm. This is particularly true when looking at G_{max} values, as shown in Fig. 10. For example, Fig. 10(b) shows how the shift in optimal excitation wavelength in brain tissue (see Fig. 7) results in a minimum gain value at 600 nm (corresponding to a relatively flat $1/G_{\lambda_{ex}}$ spectrum). However, Fig. 10(c) shows that, since highly pigmented tissues have $1/G_{\lambda_{ex}}$ spectra of similar shape for all emission wavelengths, the gain stays relatively constant, except at 700 nm. The gain increases at 700 nm due to the sudden shift of the "worst excitation wavelength" from 465 (at $\lambda_{em} < 700$ nm) to 620 nm (see Fig. 7). This is true for most highly pigmented tissues (liver, kidney, bladder, esophagus, and stomach). However, this effect is due to the increasing range of excitation wavelengths for longer emission wavelengths, and so is specific to the particular experimental setup rather than being a real spectral feature of the tissues.

6.3 Dose Reduction and Cost Implications

A clear advantage of the approach presented here is that both the threshold concentration and gain metrics allow, in principle,
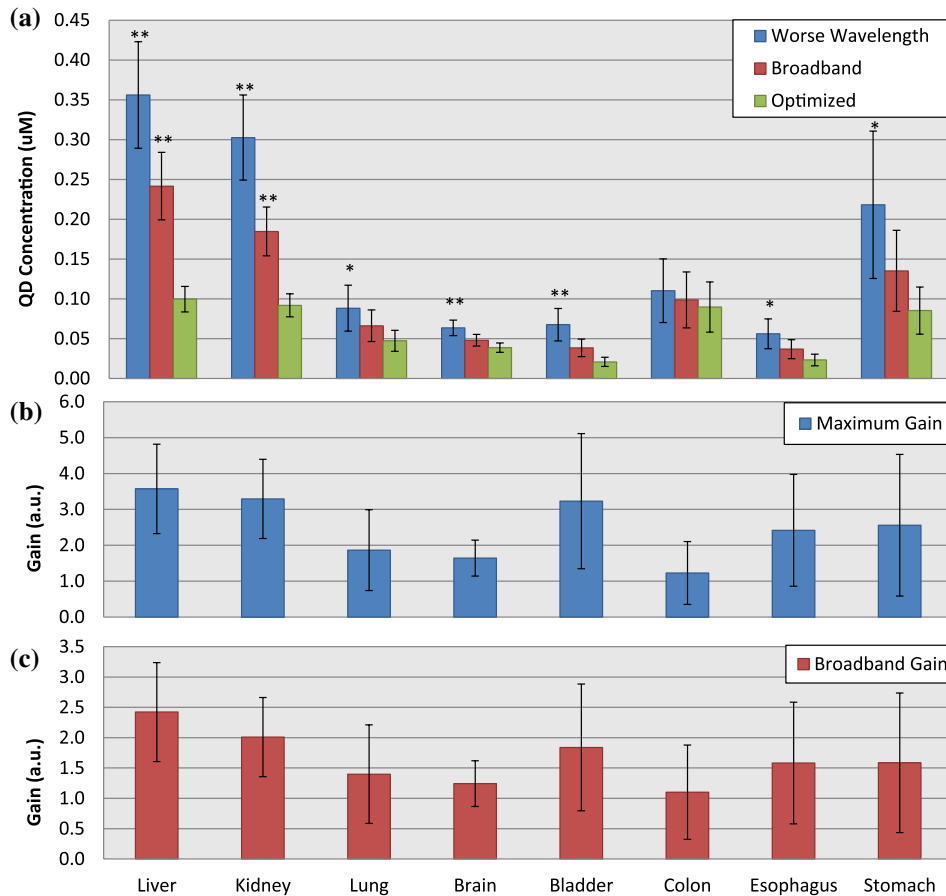
Fig. 9 (a) Estimated threshold QD600 concentration values and the corresponding (b) maximum and (c) broadband contrast optimization gain for the bulk tissues. In (a), the statistical significance of the wavelength optimization is indicated: $p < 0.01$ (**) and $p < 0.05$ (*).

direct extrapolation to address issues in QD dosimetry. Thus, significant cost and toxicity reductions could be achieved if the findings translate into reduced dose *in vivo*. For example, a 200 μL vial of 2 μM QTracker565 solution currently costs $450 (Invitrogen, Carlsbad, California, USA), and it is recommended to inject ~20 μL in a 25 g mouse for vascular imaging. Hence, if an equivalent dosage was used in a 75 kg human, then 60 mL would be required, at a cost of $>100,000$. However, based on our results for surface imaging of the esophagus, if the same procedure was done with QTracker705 using the

optimal excitation wavelength, this dose could be reduced 250-fold, for a clinical cost of only $500. Clearly then, if QDs are ever to translate to the clinic, wavelength optimization and dosimetry will be defining criterions of feasibility.

6.4 Quantitative Comparison Between Fluorescent Contrast Agents

Another potential application of the contrast optimization metrics is to establish quantitative comparison between different
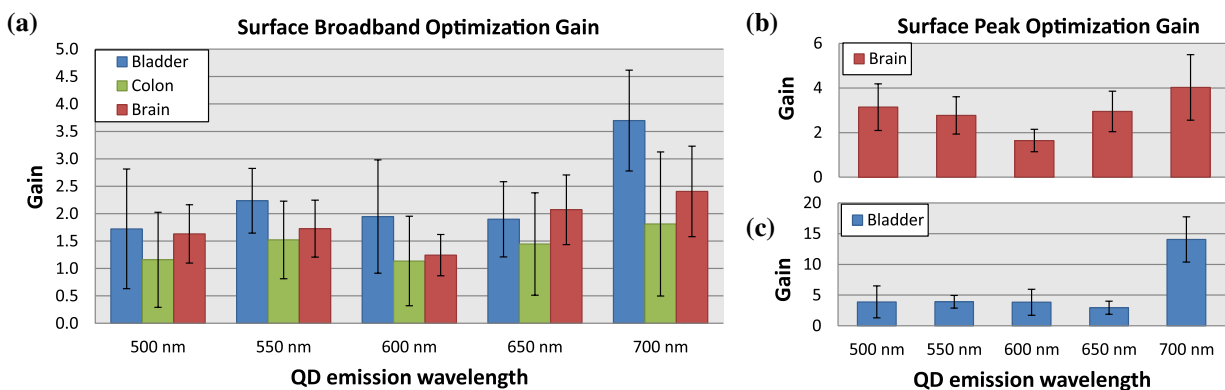
Fig. 10 (a) Estimated $G_{broadband}$ values for the intact bladder, colon and brain as a function of emission wavelength. (b) Estimated G_{max} values for the intact brain tissue, showing a drop at 600 nm that is likely due to a spectral shift in autofluorescence. (c) Estimated G_{max} values for the intact bladder, showing low variation except at 700 nm.
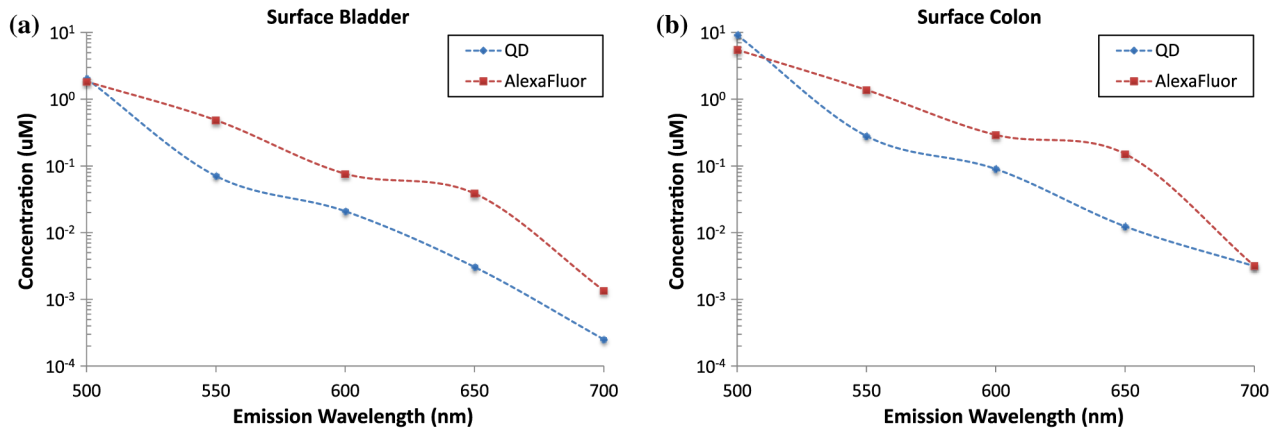
Fig. 11 Example of surface QD and AlexaFluor threshold concentration versus emission wavelength for (a) bladder tissue and (b) colon tissue. Note the logarithmic concentration scales. The lines are simply to guide the eye.

fluorescent contrast agents, such as QDs and organic fluorophores. Figure 11 shows two typical examples of QDs compared to AlexaFluor for surface imaging of bladder and colon tissue. Note that, although the threshold concentrations are similar at $\lambda_{em} = 500$ nm, they are always lower for the QDs at higher emission wavelengths. This is consistent for all tissues and, at $\lambda_{em} = 650$ nm where the difference is the greatest, the threshold QD concentration is on average 17 times lower than that of the AlexaFluor. The likely reason is that more autofluorescence is excited at wavelengths that maximize the AlexaFluor contrast in comparison to the blue-shifted wavelengths that are optimal for QD imaging. Here, the peak contrast for the AlexaFluor imaging was always obtained at the longest excitation wavelength used (450, 510, 546, 600, and 620 nm for AlexaFluor488, 532, 568, 633, and 680, respectively).

7 Discussion

7.1 Experimental Limitations

This work demonstrates, in a wide range of different tissues *ex vivo*, how the tissue optical properties markedly affect wavelength optimization for QD-based imaging. Although the results are self-consistent, caution should be taken before applying them directly *in vivo*, due to the inherent difficulties associated with *ex vivo* tissue manipulation, due to altered hydration, blood content, oxygenation and temperature. In part, these factors are

reflected in the high intra-sample variability of the autofluorescence measurements. Likewise, despite making all the measurements in the hollow organs as rapidly as possible, there were still intra-sample variations over time and optical property measurements made on a different set of similar freshly excised organs indicated some blood loss during storage and/or the imaging. Another limitation of the experimental setup was the use of a single capillary size, so that the optimal concentration estimates are specific to that target geometry. However, at least over the range where optical self-attenuation of the QDs is not significant, we would expect c_{th} values to scale inversely with capillary diameter.

In terms of the accuracy of the experiments, since the analysis involves taking several ratios of measured quantities, the errors propagate and reduce the statistical significance of the performance metrics. The main sources of errors were in the AF measurement (up to $\pm 20\%$), the absorption and reduced scattering measurements (up to $\pm 20\%$), and the QD concentration measurements ($\pm 10\%$). These also reduce the accuracy of the model predictions, as reflected by the tolerance factor of 2 derived in Sec. 4 (expected to be higher for subsurface geometry). Considering the uncertainties in the target depth of $\sim \pm 10\%$), the impact on the predicted threshold concentration is $\sim 15\%$ to 40% across the emission wavelengths, depending on the tissue optical properties. Despite these uncertainties, the approach still provides valuable guidance for applications,
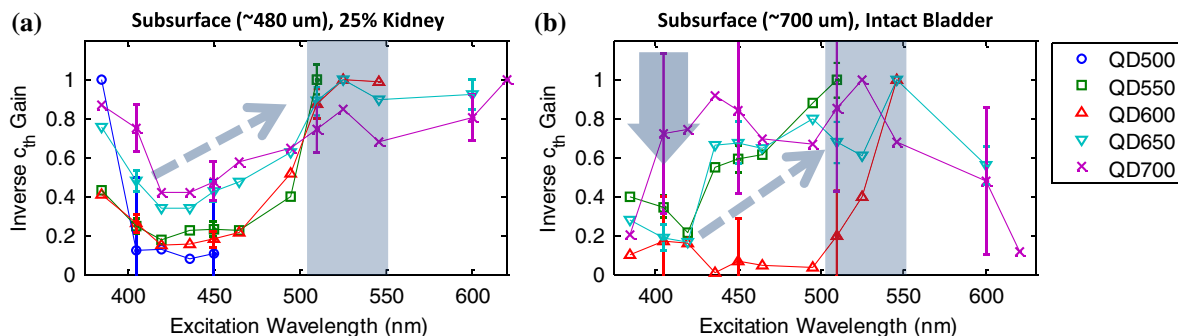
Fig. 12 Normalized contrast spectra for subsurface imaging in (a) 25% homogenized kidney and (b) intact bladder. The plain arrow illustrates suppression of the 395 to 425 nm peak and the dashed arrows highlight the red shift of the optimal excitation wavelength towards the 500 to 550 nm region (highlighted).

Table 2 Summary of photophysical parameters with respect to their impact on QD dose reduction. The arrows represent the change of parameter value (before → after) that result in QD dose reduction. For each parameter, the main factor responsible for variation of dose reduction values is included in the last row.

Parameter	λ_{em}	Depth	λ_{ex}	Tissue type	Quantum yield	Emission filter bandwidth
Change						
before	QD500	subsurface	worst	low μ_a, high AF (colon)	current	50 nm
↓	↓	↓	↓	↓	↓	↓
after	QD700	surface	optimal	high μ_a, low AF (bladder)	max(1.0)	20 nm
QD dose reduction	500 to 8000	10 to 100	~1 to 20	~4 to 9	~1.1 to 6	~1.4
Main factor	tissue AF	mucosal thickness	tissue pigmentation	λ_{em}	QD	—

considering the significant excitation wavelength optimization gain values (up to 20-fold) and the even larger benefits of using optimum emission wavelengths.

7.2 Modeling

Although the Monte Carlo model predictions were accurate across a wide parameter space, there were some problematic cases. As discussed, it is likely that the discrepancies are due to experimental factors, rather than the model breaking down. However, one clear limitation is that the tissue is modeled as a single homogenous layer. Nevertheless, reasonable agreement was still obtained even for the hollow organs, given the tolerance factor used and considering the multiple sources of experimental error, but greater precision could likely be achieved using a multi-layered Monte Carlo simulation[21,22].

As a simpler alternative to using the threshold concentration gain as the performance metric of choice, the contrast gain (i.e., a ratio of TBR values) could be used. These are equivalent as long as the signal is much higher than the autofluorescence, but when the signal is low and comparable to the AF background, the TBR values tend towards 1. This is problematic, since it then becomes impossible to differentiate between truly unstructured TBR spectra, and spectra that simply appear flat due to low signal: e.g., spectra such as those of Fig. 5 would show minimal structure if the QD concentration was significantly lower. The chosen optimization metrics do not suffer from this limitation: no matter what QD concentration c_{QD} is used for the measurements, $c_{th,best}, c_{th,broad}, G_{broadband}, G_{max}$ are the same. It is, however, still necessary to know c_{QD} to properly scale the results, as indicated by Eq. (4). Note that all the surface imaging data presented above were acquired under the high signal conditions, and thus the TBR spectra would be equivalent to the presented normalized contrast. However, this is not the case for the subsurface data, mostly acquired in low signal conditions.

7.3 Impact of Target Depth

As mentioned in Secs. 2.2 and 4.2, subsurface imaging was performed for all tissue samples, but, for the sake of brevity, the results are not reported above, since this was examined in detail in phantoms and homogenized tissues previously[10] and, as noted, most subsurface measurements suffered from lack of QD signal due to strong tissue attenuation, as considered

elsewhere.[23] Despite this suboptimal data quality, it was still possible to identify and confirm general trends on the effect of depth on wavelength optimization. Thus, in our previous work, we reported a local maximum at 500 to 550 nm (corresponding to a second hemoglobin absorption peak) in addition to the main 395 to 425 nm optimization window. It was suggested that the latter would not be sustained at depth due to the high QD signal attenuation, resulting in red shift of the optimal excitation wavelength in favor of the secondary peak. This trend was confirmed here: the 500 to 550 nm local maximum was observed in almost all cases for surface imaging (Fig. 7), and the red shift towards 500 to 550 nm was also seen in most subsurface cases, as shown in Fig. 12.

The subsurface measurements performed on hollow organs also allowed the effect of depth on the estimated threshold QD concentrations to be quantified. In general, the subsurface $c_{th,best}$ versus λ_{em} curves were parallel to the surface imaging data, suggesting little influence of the emission wavelength on signal attenuation, especially at longer wavelengths (data not shown). The attenuation factor was mostly driven by the tissue thickness and absorption coefficient at the optimal excitation wavelength. The increase in threshold concentration from surface to subsurface (for both QDs and AlexaFluor) ranged from ~10 for the colon (the thinnest and least pigmented tissue) to ~100 for the stomach (thickest).

7.4 Other Factors

In order to minimize the required dose of contrast agent, the fluorophore-to-background autofluorescence ratio must be maximized. Here, we have demonstrated that this can be achieved experimentally by selecting different excitation and emission filters. However, this exploration was limited to a specific set of filters of fixed bandwidth. In principle, imaging could be further optimized by tuning the bandwidths. Narrower filters may result in enhanced contrast if the excitation or emission spectrum of the fluorophore exhibits a sharp maximum and/or the tissue autofluorescence spectrum exhibits a sharp minimum. For example, using 20 nm rather than 50 nm bandwidth emission filters to detect the QD signal would result in ~40% increase in contrast, given the 40 nm FWHM QD emission spectrum. However, this would be at the expense of total brightness, so that the exposure times would have to be increased by ~80% to obtain the same integrated signal. Due to the relative flatness

of the QD excitation spectra, there would not be significant gains in narrowing the excitation filters, unless the autofluorescence spectrum exhibits a sharp minimum for some specific tissue. In contrast, due to their narrower excitation spectra and smaller Stokes shift, fine-tuning the filter bandwidths and central wavelengths would improve the image contrast by up to 250% for the AlexaFluor dyes.

Finally, another way to further reduce the threshold concentration would be to increase the quantum yield of the fluorophores. Since the quantum efficiency of the QDs used here ranged from 0.16 to 0.92, the potential improvement would not exceed a factor 6. A summary of the different parameters and their estimated impact on dose reduction is shown in Table 2.

8 Conclusions

The contrast optimization approach developed previously[10] has been extended and validated here against a range of bulk tissues of different optical properties and samples from hollow organs that are more directly relevant to endoscopic imaging. The overall approach appears to be valid over a broad range of tissue optical properties, the discrepancies being most likely due to experimental limitations. Using direct measurements of the tissue autofluorescence, the model accurately predicts the optimal excitation wavelength within 10 nm and the threshold concentrations within a factor 2 in over 80% of the cases. This should provide meaningful guidance for optimizing clinical applications.

Although no single optimum excitation wavelength applies to all tissues, major trends have been identified. Since the excitation spectrum of QDs is relatively flat, the optimal excitation wavelength always corresponds to a minimum in the tissue autofluorescence spectrum. Most of the tissues share common minima around 400 to 420 nm and 510 to 550 nm in AF that correspond to hemoglobin absorption peaks. Multiplexed QD imaging should be straightforward for these tissues, since there is no significant shift in optimal excitation regardless of the emission wavelength used, i.e., of the QDs. However, other tissues (e.g., lung and brain) exhibit AF spectral features that do not correlate well with blood absorption. This results in red-shifted optimal excitation for longer emission wavelengths, thus making multiplexed QD imaging harder to achieve.

With regard to contrast-optimization, the following conclusions can be drawn. Firstly, the most important parameter to consider is the emission wavelength, i.e., the QD used, since a shift of 200 nm (e.g., from 500 to 700 nm) reduces the required threshold QD concentration by orders of magnitude. Secondly, depending on the tissue and QD emission wavelength, optimizing the excitation wavelength also yields reductions in QD threshold concentration by up to 20-fold: for all tissues on average the excitation wavelength optimization gain values were $G_{max} = 5.0$ and $G_{broadband} = 1.9$. Finally, fine-tuning the filter bandwidth may yield an extra 50% contrast. In a clinical context, these results could have a significant impact, since they could potentially reduce the required dose of a promising contrast agent below toxic levels. Furthermore, a reduction of contrast agent dose directly translates into cost savings, which are substantial considering the cost of commercial QDs, even without the added cost of molecular targeting.

A broad caveat is that the actual values of the wavelength optimization gain found here may not directly translate into equivalent dose reductions in vivo. For example, in vascular imaging, the contrast agent is colocalized with blood, so that light absorption by blood may have an enhanced effect on both the signal and background. This needs to be tested and included in a full optimization model, and a follow-up study using an in vivo murine dorsal skin fold window chamber model is in progress to establish quantitative relationships between the injected QD dose, the intravascular QD concentration and the vessel-to-background image contrast. More importantly, these experiments will investigate how wavelength optimization affects the injected dose in comparison with the results presented here. In addition, this in vivo work will serve as a platform to further validate the contrast optimization model in a complex, dynamic environment that is relatively immune to the unavoidable tissue artifacts ex vivo (blood loss and deoxygenation, tissue degradation). Finally, it will also be important to follow up with more detailed studies in the endoscopically relevant subsurface geometry.

References

1. I. L. Medintz et al., "Quantum dot bioconjugates for imaging, labelling and sensing," *Nat. Mater.* **4**(6), 435–446 (2005).
2. W. C. Chan et al., "Luminescent quantum dots for multiplexed biological detection and imaging," *Curr. Opin. Biotechnol.* **13**(1), 40–46 (2002).
3. P. Diagaradjane et al., "Imaging epidermal growth factor receptor expression in vivo: pharmacokinetic and biodistribution characterization of a bioconjugated quantum dot nanoprobe," *Clin. Cancer Res.* **14**(3), 731–741 (2008).
4. S. Kim et al., "Near-infrared fluorescent type II quantum dots for sentinel lymph node mapping," *Nat. Biotechnol.* **22**(1), 93–97 (2004).
5. N. Lewinski, V. Colvin, and R. Drezek, "Cytotoxicity of nanoparticles," *Small* **4**(1), 26–49 (2008).
6. M. Roy and B. C. Wilson, "Molecular imaging with targeted quantum dot bioconjugates: the need for contrast optimisation studies," *Int. J. Nanotechnol.* **6**(5–6), 442–455 (2009).
7. Y. T. Lim et al., "Selection of quantum dot wavelengths for biomedical assays and imaging," *Mol. Imaging* **2**(1), 50–64 (2003).
8. M. Roy and B. C. Wilson, "An accurate homogenized tissue phantom for broad spectrum autofluorescence studies: a tool for optimizing quantum dot-based contrast agents," *Proc. SPIE* **6870**, 68700E (2008).
9. M. G. Muller et al., "Intrinsic fluorescence spectroscopy in turbid media: disentangling effects of scattering and absorption," *Appl. Opt.* **40**(25), 4633–4646 (2001).
10. M. Roy et al., "Homogenized tissue phantoms for quantitative evaluation of subsurface fluorescence contrast," *J. Biomed. Opt.* **16**(1), 016013 (2011).
11. B. O. Dabbousi et al., "(CdSe)ZnS core-shell quantum dots: synthesis and characterization of a size series of highly luminescent nanocrystallites," *J. Phys. Chem. B* **101**(46), 9463–9475 (1997).
12. W. W. Yu et al., "Experimental determination of the extinction coefficient of CdTe, CdSe, and CdS nanocrystals," *Chemistry of Materials* **15**(14), 2854–2860 (2003).
13. G. L. Rapaccini et al., "Gastric wall thickness in normal and neoplastic subjects: a prospective study performed by abdominal ultrasound," *Gastrointest. Radiol.* **13**(3), 197–199 (1988).

14. A. H. Blatt, J. Titus, and L. Chan, "Ultrasound measurement of bladder wall thickness in the assessment of voiding dysfunction," *J. Urol.* **179**(6), 2275–2278 discussion 2278–2279 (2008).

15. E. J. Mac Sweeney et al., "Relation of thickening of colon wall to pancreatic-enzyme treatment in cystic fibrosis," *Lancet* **345**(8952), 752–756 (1995).

16. F. Xia et al., "Observation of normal appearance and wall thickness of esophagus on CT images," *Eur. J. Radiol.* **72**(3), 406–411 (2009).

17. A. Kim et al., "A fiberoptic reflectance probe with multiple source-collector separations to increase the dynamic range of derived tissue optical absorption and scattering coefficients," *Opt. Express* **18**(6), 5580–5594 (2010).

18. R. T. Zaman et al., "Variation of fluorescence in tissue with temperature," *Lasers Surg. Med.* **43**(1), 36–42 (2011).

19. R. S. DaCosta, H. Andersson, and B. C. Wilson, "Molecular fluorescence excitation-emission matrices relevant to tissue spectroscopy," *Photochem. Photobiol.* **78**(4), 384–392 (2003).

20. X. Gao et al., "In vivo molecular and cellular imaging with quantum dots," *Curr. Opin. Biotechnol.* **16**(1), 63–72 (2005).

21. E. Pery et al., "Monte Carlo modeling of multilayer phantoms with multiple fluorophores: simulation algorithm and experimental validation," *J. Biomed. Opt.* **14**(2), 024048 (2009).

22. J. Swartling et al., "Accelerated Monte Carlo models to simulate fluorescence spectra from layered tissues," *J. Opt. Soc. Am. A. Opt. Image Sci. Vis.* **20**(4), 714–727 (2003).

23. M. Roy, "Quantitative evaluation of semiconductor nanocrystals as contrast agents for fluorescence molecular imaging," in *Medical Biophysics*, 63–72, University of Toronto, Toronto (2011).

24. J. C. Finlay and T. H. Foster, "Effect of pigment packaging on diffuse reflectance spectroscopy of samples containing red blood cells," *Opt. Lett.* **29**(9), 965–967 (2004).5

25. A. E. Burgess, "The Rose model, revisited," *J. Opt. Soc. Am. A Opt. Image Sci. Vis.* **16**(3), 633–646 (1999).